Available online at www.sciencedirect.com
ScienceDirect
Trans. Nonferrous Met. Soc. China 33(2023) 2030−2043
Transactions of Nonferrous Metals Society of China
www.tnmsc.cn

Corrosion behaviors of Mg−39Pb−11.5Al−1B−0.4Sc alloy in 3.5 wt.% NaX (X=F, Cl, Br and I) solutions

Zhi-qi FENG, Yuan SUN, Yong-hua DUAN, Hua-rong Qi, Ming-jun PENG

Faculty of Materials Science and Engineering,
Kunming University of Science and Technology, Kunming 650093, China

Received 31 January 2022; accepted 21 June 2022

Abstract: Mg−39Pb−11.5Al−1B−0.4Sc alloy was prepared by melting method, and the corrosion behaviors and mechanisms in 3.5 wt.% NaX (X = F, Cl, Br, and I) solutions were analyzed using X-ray diffraction (XRD), scanning electron microscopy (SEM), polarization curve test, and electrochemical impedance spectroscopy (EIS). The results show that the phases of Mg−39Pb−11.5Al−1B alloy are α-Mg, Mg_2Pb, $Mg_{17}Al_{12}$ and AlB_2. The addition of Sc can refine the microstructure significantly. The corrosion resistance of Mg−39Pb−11.5Al−1B−0.4Sc alloy in NaX solutions is in the order of NaCl < NaBr < NaI < NaF. During the corrosion process in NaX (X=Cl, Br, and I) solutions, Mg is first dissolved, then Mg_2Pb is dissolved, and finally $Mg_{17}Al_{12}$ is fallen off from matrix. The corrosion products of Mg and Mg_2Pb are $Mg(OH)_2$ and MgO, respectively.

Key words: Mg−39Pb−11.5Al−1B−0.4Sc alloy; halogen solutions; polarization curve; electrochemical impedance spectroscopy (EIS); microstructure; corrosion performance

1 Introduction

Magnesium (Mg) alloys have been widely used in automotive, aerospace and medical fields due to their low density, high strength, and good biocompatibility [1−3]. Lead (Pb) is of great interest due to its low cost, high density, and excellent ray linear attenuation coefficient [4,5]. Boron (B) has neutron shielding properties as well as good suppression and trapping of radiation [6]. Therefore, in order to solve the problems of interface incompatibility and poor mechanical properties caused by the large difference in density between Pb and B, a ray and neutron shielding alloy containing Mg, Pb, and B with excellent mechanical properties was developed by controlling the intermetallic phase [7,8]. This alloy has a Brinell hardness of HBS 160, a tensile strength of 105 MPa [9,10], and shielding rates are ~90% for neutrons, ~90% for X-rays, ~35% for γ-rays (in ^{60}Co sources) and ~50% for γ-rays (in ^{137}Cs sources) [11−13]. Thus, this series of shielding alloys containing Mg, Pb, and B have great potential for application as radiation shielding materials. However, a key limitation on their use is their sensitivity to corrosion, which hinders their viability in highly corrosive seawater environments. Therefore, the improvement of their corrosion resistance should be fully considered.

As is known, for Mg alloys, Sc can significantly refine grains, increase the number of grain boundaries, form high density precipitates, and improve the corrosion resistance, mechanical properties, and thermal stability [14−16]. It has been reported that Sc facilitates the deposition and removal of impurities in Mg alloys [17,18]. Therefore, in this work, 0.4 wt.% Sc was added for

Corresponding author: Yong-hua DUAN, Tel: +86-15987173606, E-mail: duanyh@kust.edu.cn;
Hua-rong QI, Tel: +86-13888513976, E-mail: qihuarong@163.com
DOI: 10.1016/S1003-6326(23)66241-7

improving the corrosion resistance of a representative Mg−39Pb−11.5Al−1B alloy.

In general, shielding materials need to work for long periods in complex corrosive conditions with neutral salt solutions [19,20]. Moreover, the corrosive environment for shielding materials is mainly cooling water containing the elements halides (F, Cl, Br, and I) [21,22]. Unfortunately, the corrosion caused by Cl^- and F^- can significantly damage the passivation film on the material's surface [23], and Cl^- and F^- ions in the cooling water cannot be completely eliminated. Besides, F^- ions can induce stress corrosion of shielding materials, and a small amount of F^- ions can increase the initial corrosion rate and hydrogen uptake of shielding materials, and increase the tendency towards hydrogen embrittlement [24]. When the cooling water contains Cl^- ions, the sensitivity of materials to pitting corrosion, stress corrosion, and crevice corrosion increases [25,26]. During the normal operation of the reactor, neither F^- ions nor Cl^- ions should exceed 0.15 mg/kg. Therefore, the content of F^-, Cl^- and other impurity ions in the reactor cooling water must be strictly controlled. Otherwise, the shielding material will be corroded and damaged, the structural bearing strength will be reduced, and a serious nuclear disaster will be caused.

The corrosion behaviors in solution containing halogens are therefore important prior to the application of nuclear shielding materials. In this work, the effect of Sc on Mg−39Pb−11.5Al−1B−0.4Sc alloy in 3.5 wt.% NaX (X=F, Cl, Br and I) solutions were investigated using X-ray diffractometer (XRD), scanning electron microscopy (SEM), polarization curve tests and electrochemical impedance spectroscopy (EIS), with the aim of further discussing its corrosion mechanisms in these four different sodium halide solutions in order to ensure safety and reliability for use in cooling water.

2 Experimental

The nominal Mg−39Pb−11.5Al−1B−0.4Sc alloy (Mg (48.1±0.01) wt.%, Pb (39±0.01) wt.%, Al (11.5±0.01) wt.%, B (1±0.01) wt.%, and Sc (0.4±0.01) wt.%) was prepared from pure Mg ((99.99±0.01) wt.%), pure Pb ((99.99±0.01) wt.%), pure Sc ((99.99±0.01) wt.%) and Al−B master alloy (B (8±0.01) wt.%, and Al (92±0.01) wt.%) using an intermediate frequency furnace under the protection by molten salt of (45±0.01) wt.% $MgCl_2$, (40±0.01) wt.% KCl, (10±0.01) wt.% NaCl, and (5±0.01) wt.% MgO. Cylindrical specimens in a size of *d*15 mm × 8 mm (±0.1 mm) were cut from the alloy bars, and then processed into a size of 10 mm × 10 mm × 10 mm (±0.1 mm). The samples were embedded in non-conductive epoxy resin molds, ground with the 1200 mesh silicon paper, polished with 2.5 μm diamond paste, and etched in a solution of (3±0.01) vol.% nitric acid and (97±0.01) vol.% absolute ethanol. X-ray diffractometer (XRD, BRUKER D8 ADVANCE Germany) and scanning electron microscope (SEM, PhilipsXL370) equipped with energy dispersive spectroscopy (EDS) were used to analyze the phase composition and microstructure of Mg−39Pb−11.5Al−1B−0.4Sc alloy.

The electrochemical test was carried out on the CS310H electrochemical workstation in (3.5±0.01) wt.% NaX (X=F, Cl, Br and I) solutions at room temperature ((23±2) °C). A conventional three-electrode system was used, in which the reference electrode was a saturated calomel electrode (SCE), the auxiliary electrode was a platinum electrode, and the working electrode was the sample with surface area of 1 cm^2. The dynamic scanning polarization curve was tested with the scanning rate of 1 mV/s from −0.9 to −1.8 V vs open circuit potential (OCP). By taking into account the peak-to-peak value in the open circuit, 10 points per decade were selected for EIS measurement. EIS was measured using the alternating current (AC) at OCP with amplitude of ±10 mV and a frequency range from 10^{-2} to 10^5 Hz. Although 1 mV/s is adopted in this stage of the experimentations, it is remarked that this selection has no provided substantial distortions on the polarization curves obtained. In this sense, it is worth noted that potential scan rate has an important role in order to minimize the effects of distortion in Tafel slopes and corrosion current density analyses, as previously reported [27−30]. ZView2 software was used to fit the impedance spectra, and the equivalent circuit diagram was obtained. In addition, XRD results before and after corrosion, OCP curves, potentiodynamic polarization curves and EIS measurements were all verified by three repeated tests.

3 Results and discussion

3.1 Microstructure and phases

Before the investigation of effect of Sc on Mg−39Pb−11.5Al−1B−0.4Sc alloy, the initial microstructure, XRD pattern and EDS results of Mg−39Pb−11.5Al−1B alloy without Sc are analyzed, and the result are shown in Fig. 1. From Fig. 1(a), in the original microstructure of the alloy without Sc, there are four types of microstructures, i.e., the thick white dendritic area marked as A, the thick dark gray area marked as B, the thin light gray area marked as C, and the black blocky area marked as D. From the XRD patterns in Fig. 1(b), it can be seen that the alloy is mainly composed of five phases, and the XRD peak intensity of Mg_2Pb is the strongest, thereby indicating that Mg_2Pb is the main phase. Meanwhile, the XRD peak of α-Mg is also more obvious. Thus, Mg−39Pb−11.5Al−1B alloy is mainly composed of Mg_2Pb (JCPDS 01-0465) and α-Mg phases (JCPDS 35-0821), as well as a small amount of $Mg_{17}Al_{12}$ (JCPDS 01-1128), Pb (JCPDS 23-0345) and AlB_2 (JCPDS 39-1483). As reported in literature using first-principles calculation [31], the formation enthalpies of Mg_2Pb, Mg and $Mg_{17}Al_{12}$ in the alloy is in a sequence of Mg > Mg_2Pb > $Mg_{17}Al_{12}$, indicating that $Mg_{17}Al_{12}$ has the best stability and the lowest corrosion tendency; while Mg has the worst stability and the highest corrosion tendency, so Mg is the easiest and the first phase in the alloy to undergo corrosion reaction. As the corrosion progresses, the amount of Mg phases decreases, and Mg_2Pb phase becomes the anode of

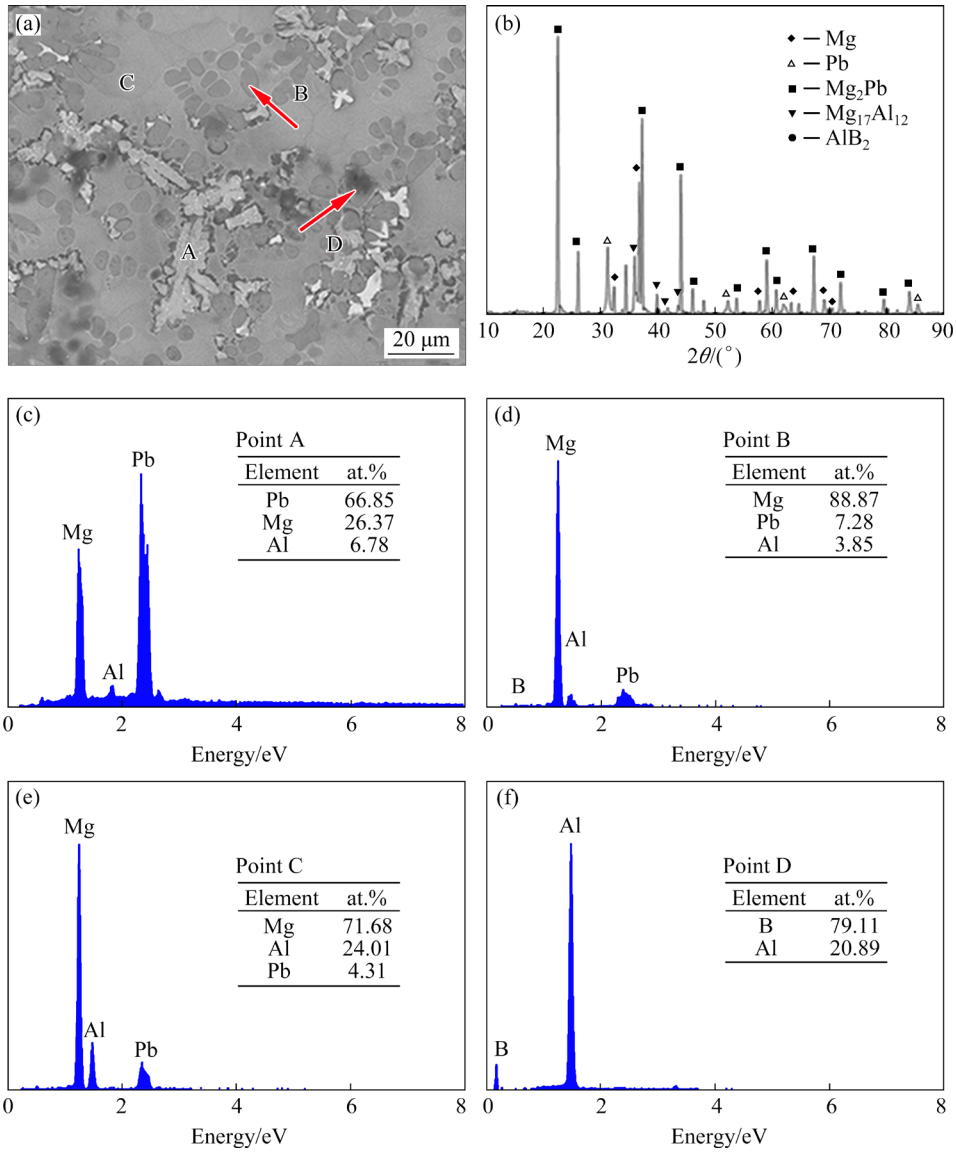

Fig. 1 SEM image (a), XRD pattern (b) and EDS results (c−f) of Mg−39Pb−11.5Al−1B alloy

the corrosion galvanic cell, and the insoluble corrosion product $Mg(OH)_2$ accumulates on the surface of the alloy to form a porous film. Then, as the porous membrane falls off, the new alloy surface is also exposed. Thus, the existence of Mg_2Pb and Mg phases in Mg−39Pb−11.5Al−1B alloy is an important factor affecting its corrosion resistance.

Figures 1(c−f) show the EDS results of the labeled points of Mg−39Pb−11.5Al−1B alloy. The EDS analysis shows that there are Mg, Al, and Pb elements at Points A, B and C, and B and Al elements at Point D. From Fig. 1(c), the composition of Point A contains mainly two elements of Mg and Pb. The molar fractions of Mg and Pb are 66.85% and 26.37%, respectively, and the ratio of Mg/Pb is larger than 2:1. Therefore, the microstructure at Point A should be Mg + Mg_2Pb eutectic. From Fig. 1(d), the molar fraction of Mg is as high as 88.87%, so the microstructure at Point B is the Mg-rich phase. From Fig. 1(e), at Point C, the molar fractions of Mg and Al are 71.68% and 24.01%, respectively, and the ratio of Mg to Al is ~2.99:1. As is known, the molar ratio of Mg/Al is ~1.42:1 in $Mg_{17}Al_{12}$. Thus, the microstructure at Point C should be Mg + $Mg_{17}Al_{12}$ eutectic. In Fig. 1(f), the Al content at Point D is much greater than that at Points A, B, and C. There are mainly Al and B elements, and the molar fractions of Al and B elements are 20.89% and 79.11%, respectively. Consequently, the microstructure at Point D is mainly AlB_2. Besides, from the results of XRD and EDS, it can be seen that B element exists in the form of AlB_2, while Pb element mainly exists in the form of Mg_2Pb. By adding the third elements of Mg and Al, Pb and B are evenly distributed in the alloy.

After adding Sc, the effect of Sc on the microstructure of Mg−39Pb−11.5Al−1B alloy is

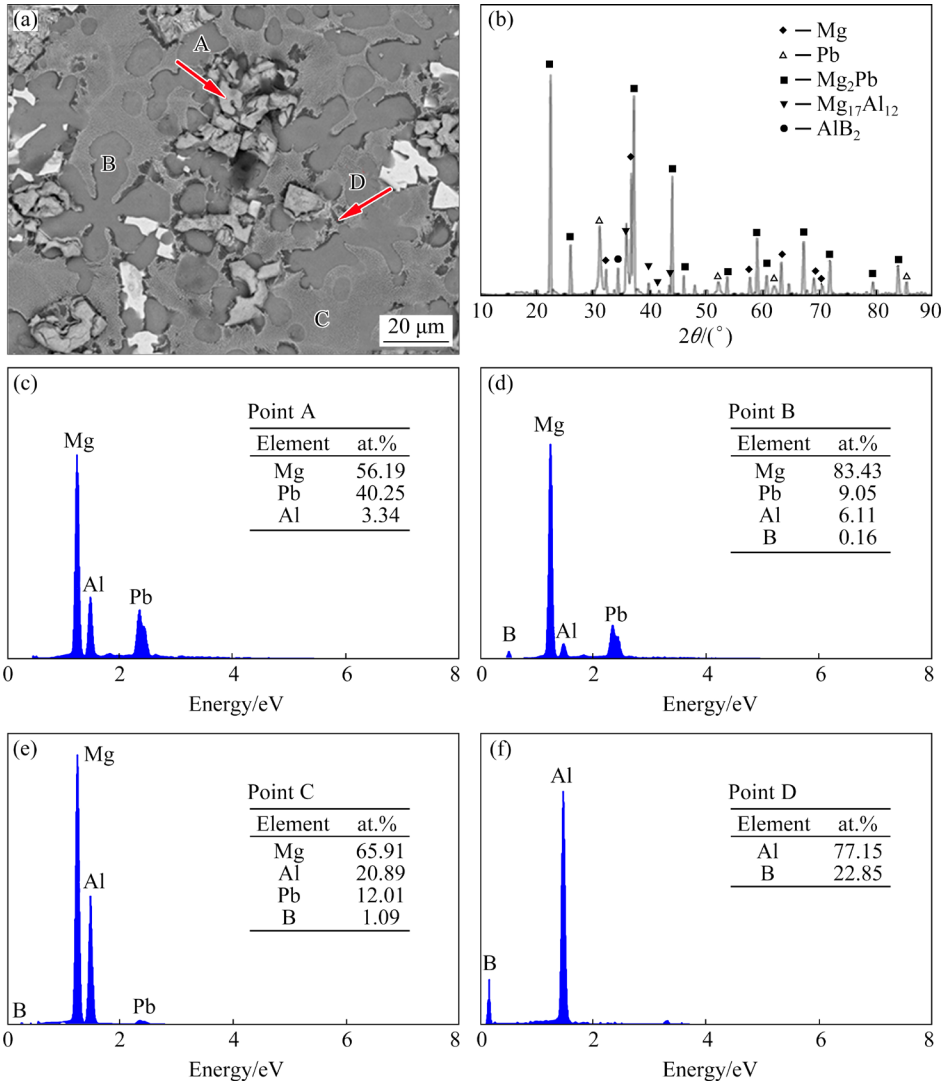

Fig. 2 SEM image (a), XRD pattern (b) and EDS results (c−f) of Mg−39Pb−11.5Al−1B−0.4Sc alloy

also analyzed. Figure 2 shows the initial microstructure, XRD patterns and EDS results of Mg−39Pb−11.5Al−1B−0.4Sc alloy. From Fig. 2(b), it can be found that, compared to Mg−39Pb−11.5Al−1B alloy, the intensity and position of the XRD peaks of phase in Mg−39Pb−11.5Al−1B−0.4Sc alloy do not change after the addition of Sc and no new XRD peaks can be found, indicating that no Sc-containing phase is formed. This may be due to the fact that the amount of Sc added to Mg−39Pb−11.5Al−1B alloy is very small (only 0.4 wt.%) and fails to form a new phase containing Sc, or the amount of new phase containing Sc formed is too small to be detected by the X-ray diffractometer. Compared to Fig. 1(a), the coarse white dendritic region with the composition of Mg + Mg_2Pb in Fig. 2(a) becomes much finer, and the dispersion and homogeneity of the α-Mg matrix are higher.

Figure 3 shows the SEM image of microstructure of Mg−39Pb−11.5Al−1B−0.4Sc alloy and the EDS images of the corresponding elements. As expected, Mg, Pb, B, and Sc elements are uniformly distributed in the alloy. As for Al element, the microstructure on the top right in Fig. 3(a) is Mg + Mg_2Pb eutectic, and the compositions of Mg, Pb, and Al herein are 56.19 at.%, 40.25 at.%, and 3.34 at.%, respectively.

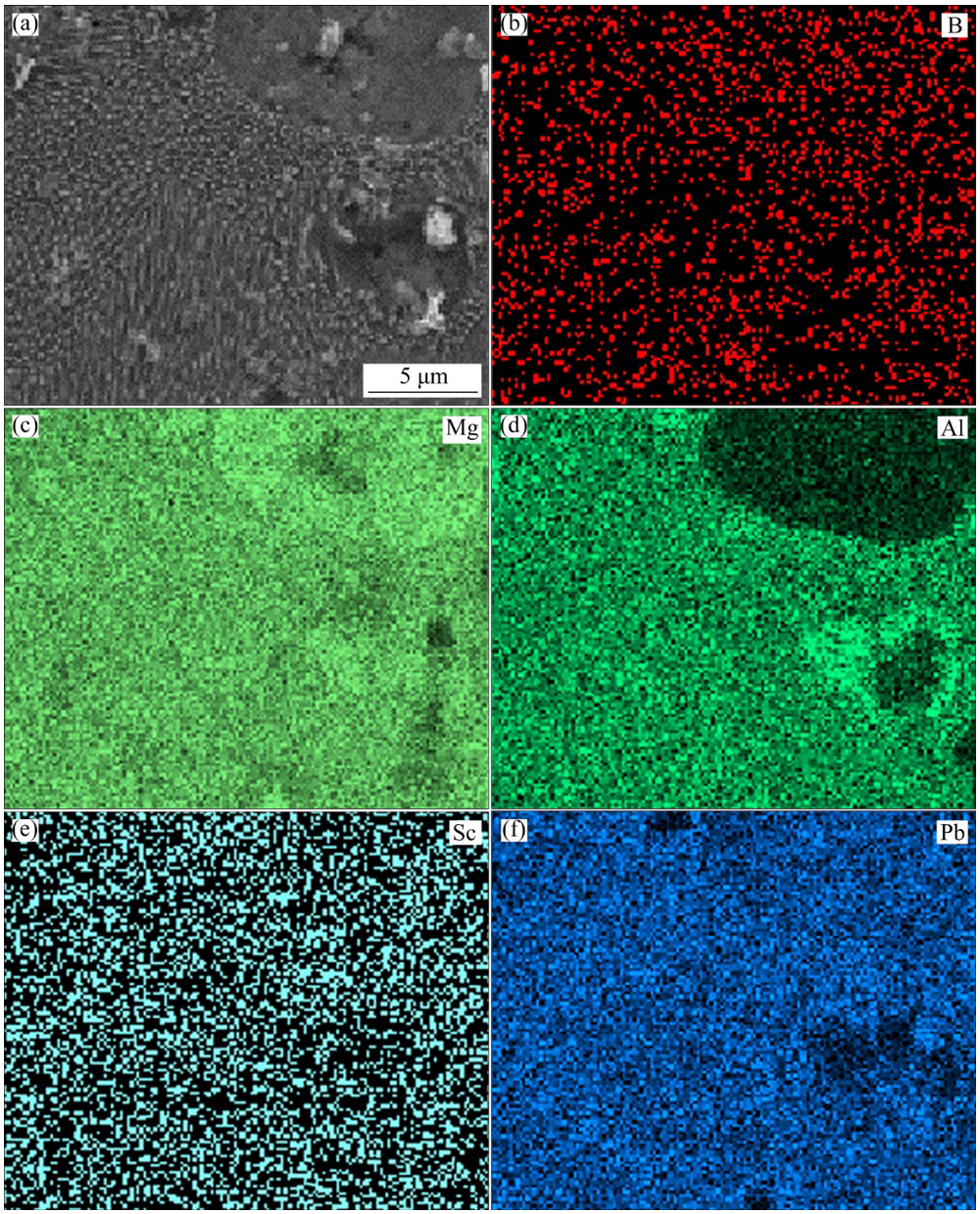

Fig. 3 SEM image (a) and EDS mappings (b−f) for Mg−39Pb−11.5Al−1B−0.4Sc alloy

3.2 Electrochemical measurements

Figure 4(a) depicts the OCP curves of Mg−39Pb−11.5Al−1B−0.4Sc alloy in 3.5 wt.% NaX (X=F, Cl, Br, and I) solution. The OCP is the potential difference between the working electrode and the reference electrode when there is no load, and it can be used to describe the surface state of the sample electrode [32−34]. The OCP curves generally have three phases: a slow-rising phase, a fast-rising phase, and a stable phase. From Fig. 4(a), the OCP of Mg−39Pb−11.5Al−1B−0.4Sc alloy in the 3.5 wt.% NaF solution is about −1.0 V. There are substantial discrepancies in the details of the OCP of the other three solutions. According to the OCP theory, the more positive the OCP is, the less the corrosion tendency is, which can roughly indicate that the alloy has less corrosion tendency in NaF solution. The measurements of OCP curves of Mg−39Pb−11.5Al−1B−0.4Sc alloy in 3.5 wt.% NaX (X=F, Cl, Br, and I) solution were conducted, and the results are shown in Fig. S1 in Supporting Materials. The change trend of OCP curves in Fig. S1 is similar to that of OCP curves in Fig. 4(a), indicating that the results of OCP can be duplicated.

The OCP of Mg−39Pb−11.5Al−1B−0.4Sc alloy in 3.5 wt.% NaF solution is preliminarily divided into three stages. (1) Stage *AB*: The potential in the first 100 s starts to drop from −1.19 V. This is the dissolution stage of surface corrosion inhibitor formed by the oxidation of Mg−39Pb−11.5Al−1B−0.4Sc alloy. When the processed sample is put into the NaF solution, the oxide film on the surface of the alloy is immediately dissolved, making the alloy matrix exposed and quickly showing the intrinsic electrode potential for the alloy matrix. However, the intrinsic electrode potential of the alloy matrix is much lower than the electrode potential when there is a surface corrosion inhibitor. Therefore, the potential shifts sharply in the negative direction and is reduced to −1.62 V. (2) Stage *BC*: With the dissolution of Mg−39Pb−11.5Al−1B−0.4Sc sample,

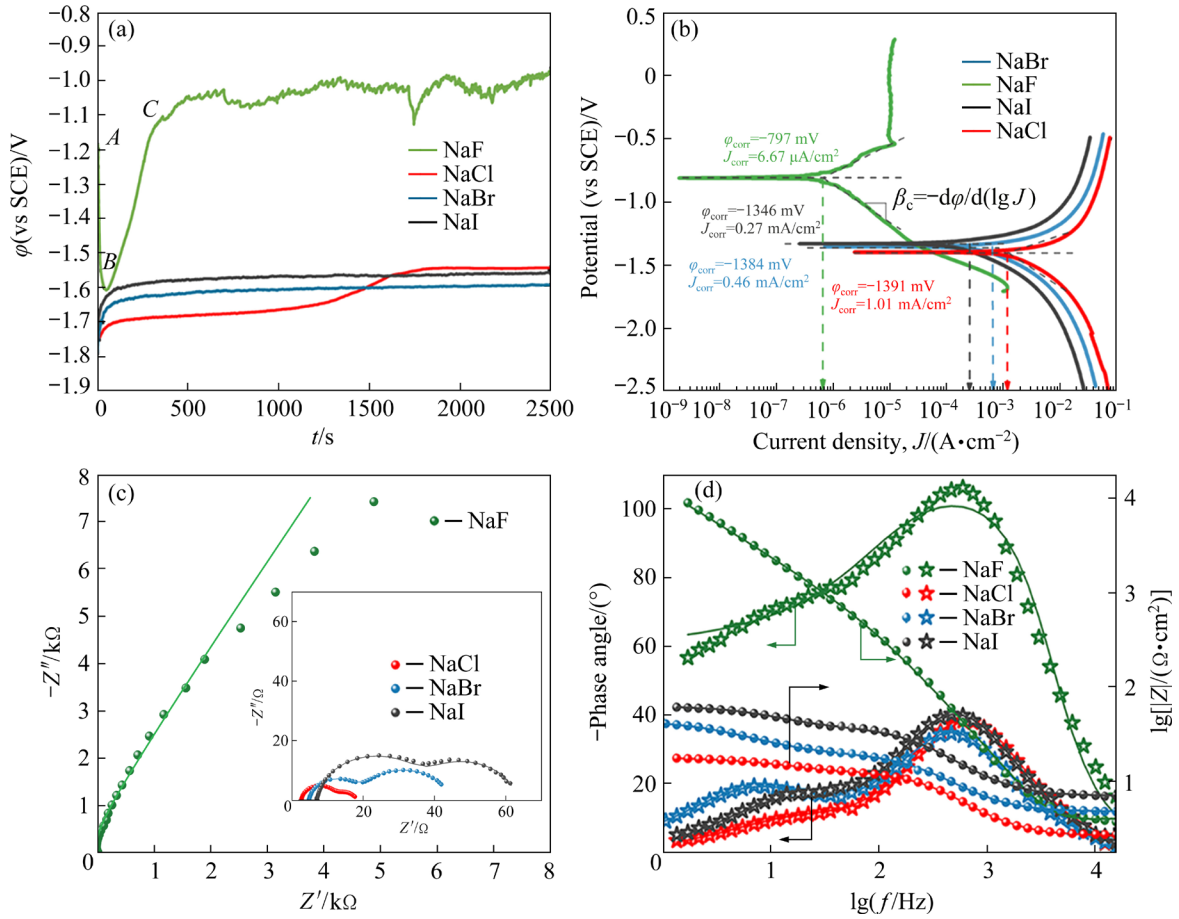

Fig. 4 Electrochemical test results of Mg−39Pb−11.5Al−1B−0.4Sc alloy in 3.5wt% NaX (X=F, Cl, Br, and I) solution: (a) OCP curves; (b) Polarization curves; (c) Nyquist diagram (The points are experimental values, and the solid lines are the fitting results); (d) Bode diagram (The solid points are the experimental values of the Bode diagram, the pentagram points are the experimental values of the Bode-phase diagram, and the solid lines are the fitting results)

the total concentration of metal ions on the surface of the sample rises, so the OCP curve rises rapidly from −1.62 to −1.05 V in the next 400 s. The anode process is suppressed in this process, and the potential moves in the positive direction. (3) After Point *C*: The dissolution of the sample surface reaches a dynamic equilibrium, no obvious fluctuations occur, and finally a stable electric potential is reached, about −1.0 V. In addition, the *AB* segment cannot be detected in the test of the other three halogen element aqueous solutions. This is because the electrochemical test is started after the sample is pretreated. During this period, the interval is very short, and the oxide formed in a short time is very thin, or the occurrence of *AB* segment cannot be detected because this stage proceeds so fast. The initial process of the *AB* segment is very short and does not affect the charging capacitance of the electric double layer.

Figure 4(b) shows the potential polarization curve after Mg−39Pb−11.5Al−1B−0.4Sc alloy is immersed in 3.5 wt.% NaX (X=F, Cl, Br, and I) solutions for 40 min. With continuous scanning from the cathode to the anode, the magnesium of the anode branch loses electrons and is dissolved by the anode, and the cathode branch undergoes a hydrogen evolution reaction. From Fig. 4(b), one can see that the four $\varphi-\lg J$ curves show a linear relationship in Tafel zone. During the potentio-dynamic polarization process, the polarization curve in NaF solution has an obvious passivation platform, indicating that a dense passivation film is formed on the corroded surface. Except in NaF solution, the polarization curves in the other three corrosion solutions exhibit similar corrosion behavior, which can be the consequence of almost the same electrochemical reaction. This shows that, compared to NaF solution, Mg−39Pb−11.5Al−1B−0.4Sc alloy is more susceptible to the corrosion in the other three solutions.

The Tafel linear extrapolation method [35,36] is used to obtain the kinetic parameters, and the calculated corrosion potential (φ_{corr}) and corrosion current density (J_{corr}) are listed in Table 1. The intersection of the self-corrosion potential and the anode Tafel line is used to determine the self-corrosion current density. To eliminate or compensate for the influence of solution resistance, the IR compensation function of CS Studio5 is used. φ_{corr} can reflect the corrosion tendency of the alloy. The more positive φ_{corr} corresponds to the smaller corrosion tendency, which is consistent with the results of the polarization curve. The corrosion rate of the alloy can be calculated according to J_{corr}. The greater J_{corr} reflects the worse corrosion resistance. From Table 1, the order of corrosion resistance of Mg−39Pb−11.5Al−1B−0.4Sc alloy in the 3.5 wt.% NaX (X = F, Cl, Br, and I) solutions is NaF > NaI > NaBr > NaCl.

Table 1 Polarization curve fitting parameters of Mg−39Pb−11.5Al−1B−0.4Sc alloy in 3.5 wt.% NaX (X= F, Cl, Br and I) solutions

Solution	φ_{corr}/V	J_{corr}/(A·cm^{-2})
NaF	−0.79674±0.03	(6.6646±0.02)×10^{-7}
NaCl	−1.3909±0.007	(1.0064±0.02)×10^{-3}
NaBr	−1.3842±0.01	(4.604±0.02)×10^{-4}
NaI	−1.3458±0.02	(2.7449±0.02)×10^{-4}

The important role of the electrochemical impedance spectroscopy (EIS) is to characterize the electric double layer formed at the electrode/electrolyte interface [37]. A sinusoidal signal X of different frequencies and small amplitudes is compared with the unique response signal Y obtained from the system after interference. There is a linear relationship between the two signals, that is, $Y=X\cdot G(\omega)$, where the transfer function $G(\omega)$ is used to describe the relationship between the sinusoidal signal and the response signal. $G(\omega)$ is also a function of the angular frequency ω, which is the impedance Z. The impedance Z can be expressed as follows:

$$Z(\omega)=Z'(\omega)+jZ''(\omega) \quad (1)$$

In a coordinate diagram, the length from the origin of the coordinates to a point on the function is called the impedance modulus $|Z|$, and the angle between that point and the origin and the x-axis is called the phase angle ϕ of the impedance, which can be obtained from the following equations:

$$|Z|=\sqrt{Z'^2+Z''^2} \quad (2)$$

$$\phi=\arctan(-Z''/Z') \quad (3)$$

At the OCP state, the Nyquist diagram of Mg−39Pb−11.5Al−1B−0.4Sc alloy in 3.5 wt.% NaX (X=F, Cl, Br, and I) solutions is shown in Fig. 4(c). Obviously, the Nyquist diagram of the alloy in NaF solution is different from that in the

other three solutions, indicating that the corrosion mechanism of the alloy in NaF solution is different from that in the other three solutions. In NaF solution, only the effective capacitance of electric double layer exists, and the corrosion resistance is the best. The impedance spectra of the alloy in the other three solutions show two capacitive reactance arcs in the frequency range, that is, the effective capacitance of electric double layer and the effective capacitance of corrosion film. The capacitance arc in high-frequency region is related to charge transfer reaction [38], which indicates that the surface of the alloy is always in an active dissolution state in NaCl, NaBr, and NaI solutions. In addition, the capacitive reactance arc radius can reflect the magnitude of the charge transfer resistance. The capacitor arc in the middle and low frequency regions is related to the accumulation of corrosion products on the alloy surface [39]. Among them, the arc-resistant radius of the alloy in 3.5 wt.% NaCl solution is the smallest, and the arc-resistant radius of the alloy in 3.5 wt.% NaI solution is the largest. The larger the anti-capacitance arc radius is, the larger the impedance and the better the corrosion resistance are. Consequently, the corrosion resistance is in the order of NaF > NaI > NaBr > NaCl.

Figure 4(d) shows the Bode diagram. The phase angle of the alloy has the same trend as the semicircle diameter of the capacitor [40,41]. Mg−39Pb−11.5Al−1B−0.4Sc alloy has the highest corrosion resistance in 3.5 wt.% NaF solution. Moreover, the maximum phase angle is in the order of NaCl < NaBr < NaI < NaF solutions. The maximum phase angle close to 90° indicates that a complete and dense passivation film is formed on the corroded surface. A smaller maximum phase angle indicates that the corrosion product film is more incomplete and porous. The phase angle of the alloy in 3.5 wt.% NaF solution is as high as 106°, indicating that a complete and dense passivation film is formed on the corroded surface. The second maximum phase angle corresponds to 3.5 wt.% NaI solution with the maximum phase angle of 40°. The corrosion resistance of the alloy in 3.5 wt.% NaF solution is much greater than that of the other three halogen-containing solutions, which is in good agreement with the polarization curve results. In summary, the corrosion resistance of Mg−39Pb−11.5Al−1B−0.4Sc alloy in the four halogen-containing solutions follows the order of NaF > NaI > NaBr > NaCl.

In order to further obtain the corrosion mechanism, the impedance spectrum is analyzed by Zview 2 software. Figure 5 shows the fitted equivalent circuits of Mg−39Pb−11.5Al−1B−0.4Sc alloy. In the equivalent circuit, R_s is solution resistance, CPE_{dl} is corrosion double layer, CPE_f is capacitance of electrode indicating the corrosion layer, R_{ct} is charge transfer resistance, and R_f is corrosion product film resistance. Figure 5(a) shows the equivalent circuit of the alloy in 3.5 wt.% NaF solution, which is distinct from the other three halogen-containing solutions (Fig. 5(b)). The obvious difference in equivalent circuit in these solutions once again fully confirms that the corrosion mechanism of Mg−39Pb−11.5Al−1B−0.4Sc alloy in NaF solution differs from that in the other three solutions.

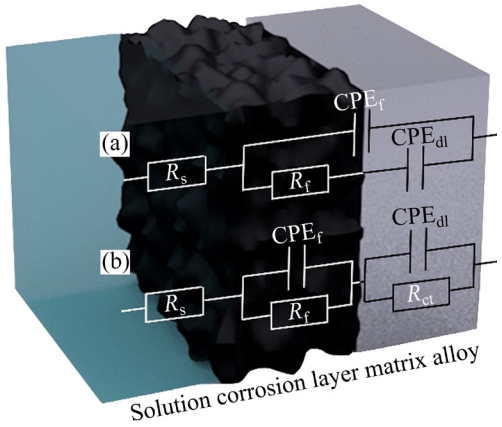

Fig. 5 Equivalent circuit diagram: (a) 3.5 wt.% NaF; (b) 3.5 wt.% NaX (X=Cl, Br, I)

The formation of the corrosion products is accompanied by the formation of corrosion film, which can hinder the diffusion of interface ions, and the corrosion film capacitance is represented by CPE_f. At present, the commonly used phase angle element (CPE) is used to fit impedance data in the equivalent circuit. The effective capacitance C_{dl} and the dielectric capacitance C_f of the electric double layer can be calculated by

$$C_{dl} = Y_{01}^{1/n}(1/R_s + 1/R_{ct})^{\frac{n-1}{n}} \quad (4)$$

$$C_f = Y_{02}^{1/n}[R_s R_f/(R_s + R_f)]^{\frac{1-n}{n}} \quad (5)$$

The specific parameters of above components

and the circuit components in the equivalent circuit are given in Table 2. As can be seen from Table 2, the solution resistance (R_s) values of different solutions are different, which is due to the various interfacial contact resistances between the electrode and the electrolyte in different solutions [42−46]. The charge transfer resistance (R_{ct}) reflects the characteristics of the electric double layer formed between the alloy and the corrosive medium. The larger the R_{ct} value is, the slower the anode dissolution in the system is, that is, the better the corrosion resistance. In Table 2, compared to the other three halogen-containing solutions, the R_{ct} value of Mg−39Pb−11.5Al−1B−0.4Sc alloy immersed in 3.5 wt.% NaF solution shows a significant increase, reaching 535.9 Ω/cm^2. This indicates that the immersion surface of Mg−39Pb−11.5Al−1B−0.4Sc alloy in 3.5 wt.% NaF solution has only a small amount of charge transfer and almost does not dissolve. The accumulation characteristics of corrosion products on the alloy surface are measured by R_f, and the corrosion products only exist in 3.5 wt.% NaX (X=Cl, Br, and I) solutions. This is because, in 3.5 wt.% NaF solution, the corrosive agent accumulates on the surface and the sample is hardly corroded. It can be seen from Table 2 that the R_f value measured in NaCl solution is relatively large, indicating that Mg−Pb−Al−B−0.4Sc alloy generates the most corrosion products and has the worst corrosion resistance in NaCl solution. During the corrosion process, these loose and porous corrosion products will be deposited on the corroded surface, making the corroded surface rougher, and further increasing the actual area due to the deposition of corrosion products.

Therefore, the surface parameter (n_1) is usually used to describe the surface characteristics. The larger value of n_1 indicates that the surface is highly uniform. Moreover, n_1 is affected by uneven current distribution caused by surface roughness and surface corrosion products. The fitting n_1 values in Table 2 show that n_1 gradually increases from NaCl, NaBr, and NaI to NaF solutions. The largest value of n_1 is for Mg−Pb−Al−B−0.4Sc alloy (1.222) immersed in 3.5 wt.% NaF solution, which also confirms that the corroded surface in 3.5 wt.% NaF solution is more compact than others. In this solution, the alloy exhibits the highest corrosion resistance. In the other three halogen-containing solutions, the n_1 values are all less than 1. Besides, the corroded surface of Mg−39Pb−11.5Al−1B−0.4Sc alloy immersed in 3.5 wt.% NaCl solution is the roughest and the most uneven. Thus, the corrosion resistance of Mg−39Pb−11.5Al−1B−0.4Sc alloy in these four solutions is in a sequence of NaF > NaI > NaBr > NaCl.

3.3 Corrosion morphology

3.3.1 Corrosion surface

Figure 6 shows the morphologies of corroded surface of Mg−39Pb−11.5Al−1B−0.4Sc alloy in 3.5 wt.% NaX (X = F, Cl, Br, and I) solutions. From Fig. 6, the alloy is slightly corroded in 3.5 wt.% NaF solution, the grain boundary morphology is clear, and the surface corrosion products are less. In NaCl, NaBr, and NaI solutions, the degree of corrosion is serious, and surface corrosion products can be clearly observed. The corrosion potential for each phase in the alloy is different, and the degree of corrosion is also different. Since α-Mg phase has the lowest corrosion potential, it is easy to form a corrosion galvanic cell with Mg_2Pb. Therefore, α-Mg should be corroded first, which also confirms the corrosion degree of the phase in the microstructure of Fig. 6.

In addition, energy spectroscopy (EDS) is carried out on Points A, B and C of the corrosion products in Fig. 6, and the EDS results are listed in Table 3. The EDS results for Point A show that

Table 2 Fitting parameters of AC impedance of Mg−39Pb−11.5Al−1B−0.4Sc alloy

Solution	R_s/ (Ω·cm^2)	R_{ct}/ (Ω·cm^2)	CPE_{dl}		R_f/ (Ω·cm^2)	CPE_f		C_{dl}/ (μF·cm^2)	C_f/ (μF·cm^2)
			Y_{01}/ (μΩ·s^n·cm^{-2})	n_1		Y_{02}/ (μΩ·s^n·cm^{-2})	n_2		
NaF	4.316	535.9	0.96777	1.222		23.032	0.66083	91.97	
NaCl	2.744	6.393	5.2799×10^3	0.78645	9.118	68.552	0.97709	1517.6	57.3228
NaBr	3.867	26.8	2.7913×10^3	0.80074	13.48	71.537	0.942917	918.7	48.9201
NaI	4.111	27.1	1.0431×10^3	0.8933	29.06	38.396	0.94111	564.7	24.9029

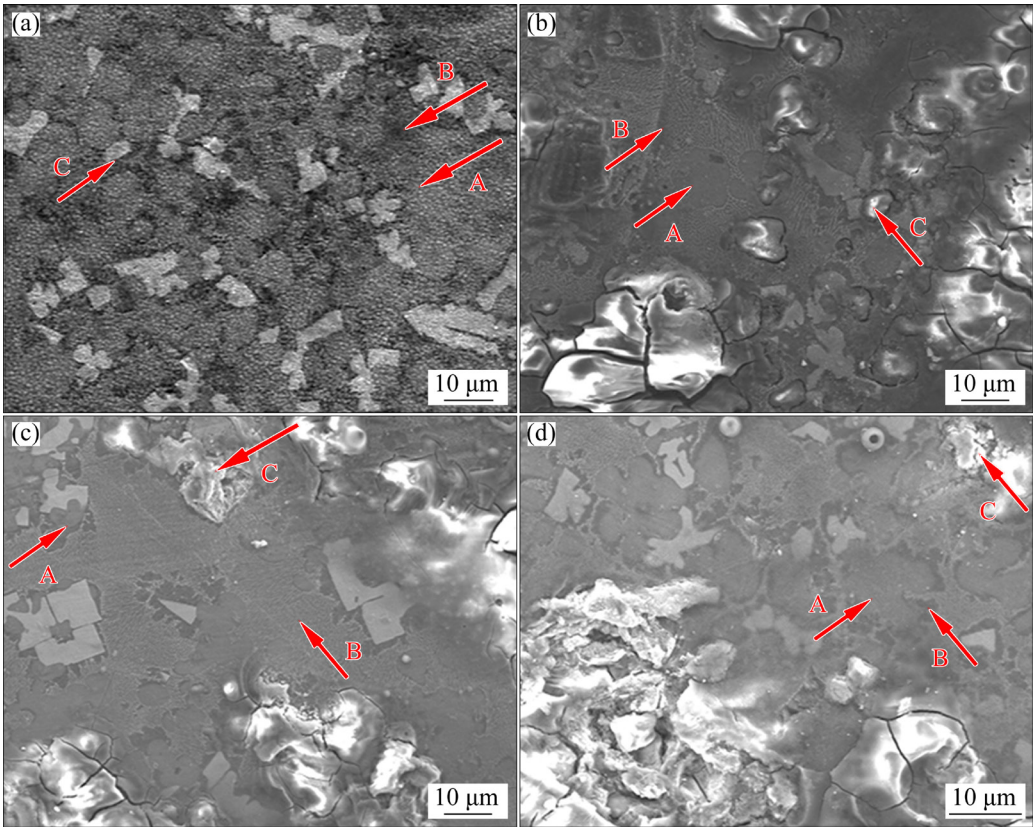

Fig. 6 Corroded surface morphologies of Mg−39Pb−11.5Al−1B−0.4Sc alloy in 3.5 wt.% NaX (X=F, Cl, Br and I) solutions: (a) NaF; (b) NaCl; (c) NaBr; (d) NaI (A: α-Mg + MgO, B: $Mg_{17}Al_{12}$, C: Mg_2Pb + a lot of MgO)

some Mg is corroded. The EDS results for Point B shows that the atomic ratio of Mg to Al is larger than 17:12, which indicates that $Mg_{17}Al_{12}$ is hardly corroded. The microstructure corresponding to Point C is Mg_2Pb, and after corrosion, the fraction of O atoms at Point C increases, and only a small amount of Pb atoms are found, indicating that the corrosion product of Mg_2Pb is MgO. Thus, Mg is dissolved first to undergo displacement reaction with NaX (X = Cl, Br, and I), and the corrosion products are concentrated near Mg_2Pb.

3.3.2 Corrosion products

The corrosion products are also analyzed through the XRD analysis to determine their composition on the surface of Mg−39Pb−11.5Al−1B−0.4Sc alloy, and the XRD results are shown in Fig. 7. Besides the main initial phases of the alloy, the corrosion products are mainly composed of $Mg(OH)_2$ and MgX_2 (X=F, Cl, Br, and I). Compared to the XRD patterns of the alloy in NaCl, NaBr, and NaI solutions, the XRD pattern in NaF solution shows that the XRD peaks of Mg_2Pb are still the strongest, while those of Pb are obviously the weakest. This is because Mg_2Pb phase is difficult to be corroded in NaF solution. In the other three solutions, the XRD peaks of MgX_2 ($MgCl_2$: JCPDS 25-1156, $MgBr_2$: JCPDS 15-0836, MgI_2: JCPDS 34-0597) and $Mg(OH)_2$ (JCPDS 44-1482) are

Table 3 EDS results of Points A, B and C of Mg−39Pb−11.5Al−1B−0.4Sc alloy in 3.5 wt.% NaX (X=F, Cl, Br and I) solutions (at.%)

Solution	Point	Mg	O	Al	Pb
NaF	A	80.1		6.18	13.72
	B	65.34		20.96	13.7
	C	57.11		2.63	40.26
NaCl	A	78.1	11.64	5.48	4.16
	B	48.54		46.2	5.26
	C	61.12	30.39	4.89	3.6
NaBr	A	75.83	16.38	6.74	3.14
	B	50.23		45.2	4.57
	C	67.5	32.5		
NaI	A	65.37	28.11	3.57	2.95
	B	55.92		42.07	2.01
	C	62.5	27.68	5.62	3.9

observed, and the XRD peaks of Mg are relatively low, meaning that Mg is dissolved and reacts with X^- and OH^- ions to form $Mg(OH)_2$ and MgX_2. It is worth noting that Mg is not observed in NaCl solution, indicating that Mg is completely dissolved. Moreover, the XRD peaks of $Mg_{17}Al_{12}$ do not change significantly in these four solutions. Figure S2 in Supporting Materials shows the XRD patterns of corrosion products of Mg−39Pb−11.5Al−1B−0.4Sc alloy after corrosion experiments. It can be seen that the corrosion products are the same as those in Fig. 7, thereby indicating that the results are duplicate and reliable.

According to the ionic radius size, the mobility of Cl^-, Br^- and I^- ions is significantly smaller than that of F^- ion [47]. The effect of X^- ions on Mg−39Pb−11.5Al−1B−0.4Sc alloy can be preliminarily divided into two aspects. The first is that X^- (X=Cl, Br, and I) ions can be adsorbed on MgO surface and cause $Mg(OH)_2$ to become more soluble MgX_2 [48]. The second is that, in the three NaX (X=Cl, Br, and I) solutions, the X^- ions can penetrate into the oxide film, and Mg_2Pb starts to be dissolved in the presence of the corrosive medium. In NaF solution, however, Mg_2Pb phase is difficult to be corroded due to the fact that the oxide film is difficult to break in this corrosive medium.

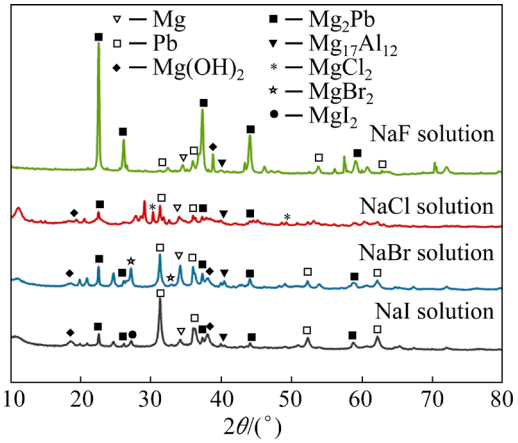

Fig. 7 XRD patterns of corrosion products of Mg−39Pb−11.5Al−1B−0.4Sc alloy

From the OCP curve, polarization curve, EIS value, corrosion surface morphology and corrosion products, the corrosion mechanism of Mg−39Pb−11.5Al−1B−0.4Sc alloy can be discussed. Figure 8 shows the schematic diagram of the corrosion mechanism of Mg−39Pb−11.5Al−1B−0.4Sc alloy immersed in NaX solutions. When the corrosion starts, Mg phase first undergoes an anodic reaction: $Mg \rightarrow Mg^{2+} + 2e$, while Mg^{2+} ions in the solution are transferred: $Mg^{2+} + 2OH^- \rightarrow Mg(OH)_2$, $Mg^{2+} + 2X^- \rightarrow MgX_2$. The cathodic reaction of dissolved oxygen corresponding to the reduction reaction occurs: $2H_2O + 2e \rightarrow 2OH^- + H_2\uparrow$. Secondly, considering the grain size, microstructure and protective properties of the corrosion product film, it is also likely that the corrosion rate of Mg−39Pb−11.5Al−1B−0.4Sc alloy is influenced by the corrosion resistance that increases with increasing Sc concentration. However, this is only an ideal prediction and further research is required.

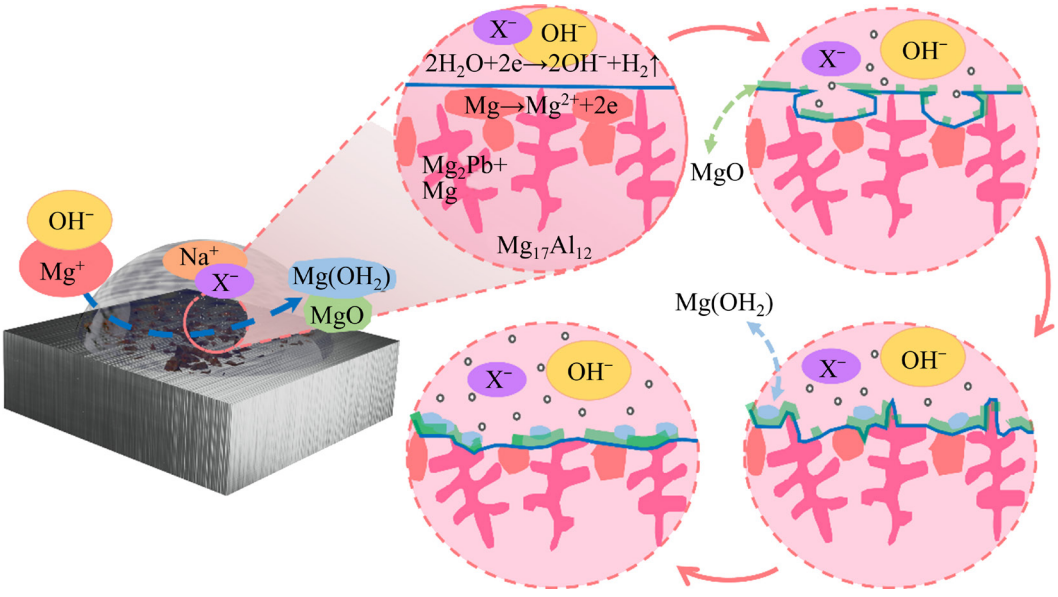

Fig. 8 Schematic diagram of corrosion mechanism of Mg−39Pb−11.5Al−1B−0.4Sc alloy

4 Conclusions

(1) Mg−39Pb−11.5Al−1B−0.4Sc alloy consists of α-Mg, Mg_2Pb, $Mg_{17}Al_{12}$ and AlB_2, and compared to Mg−39Pb−11.5Al−1B alloy, it has the smaller grain size and more uniform composition distribution.

(2) The order of corrosion resistance of Mg−39Pb−11.5Al−1B−0.4Sc alloy is NaCl < NaBr < NaI < NaF.

(3) When the corrosion starts, the Mg phase first undergoes an anodic reaction: $Mg \rightarrow Mg^{2+} + 2e$, while the cathodic reaction of dissolved oxygen corresponding to the reduction reaction occurs: $2H_2O + 2e \rightarrow 2OH^- + H_2\uparrow$.

(4) In NaX (X = Cl, Br, and I) solutions, Mg is first dissolved during the corrosion process, then Mg_2Pb is dissolved, and finally $Mg_{17}Al_{12}$ is fallen off from matrix. After Mg and Mg_2Pb are corroded, the corrosion products concentrated near Mg_2Pb are $Mg(OH)_2$ and MgO.

Acknowledgments

The authors are grateful for the financial supports from the National Natural Science Foundation of China (No. 51761023).

Supporting Information

Supporting Information in this paper can be found at: http://tnmsc.csu.edu.cn/download/07-p2030-2022-0121-Supporting_Information.pdf.

References

[1] WENG Wei-jie, BIESIEKIERSKI A, LI Yun-cang, DARGUSCH M, WEN C. A review of the physiological impact of rare earth elements and their uses in biomedical Mg alloys [J]. Acta Biomaterialia, 2021, 130: 80−97.

[2] YE Cheng-hong, XI Ting-fei, ZHENG Yu-feng, WANG Shu-qin, LI Yang-de. In vitro corrosion and biocompatibility of phosphating modified WE43 magnesium alloy [J]. Transactions of Nonferrous Metals Society of China, 2013, 23: 996−1001.

[3] GOGHERI M S, KASIRI-ASGARANI M, BAKHSHESHI-RAD H R. Mechanical properties, corrosion behavior and biocompatibility of orthopedic pure titanium−magnesium alloy screw prepared by friction welding [J]. Transactions of Nonferrous Metals Society of China, 2020, 30: 2952−2966.

[4] HU Guang, SHI Guang, HU Hua-si, YANG Quan-zhan, YU Bo, SUN Wei-qiang, Development of gradient composite shielding material for shielding neutrons and gamma rays [J]. Nuclear Engineering and Technology, 2020, 52: 2387−2393.

[5] MIJATOVIĆ T, SZILNER S, CORRADI L, MONTANARI D, POLLAROLO G, FIORETTO E, GADEA A, GOASDUFF A, JELAVIĆ MALENICA D, MĂRGINEAN N, MONTAGNOLI G, SCARLASSARA F, SOIĆ N, STEFANINI A M, UR C A, VALIENTE-DOBÓN J J. Study of the cross section determination with the PRISMA spectrometer: The 40 Ar + 208 Pb case [J]. The European Physical Journal A, 2016, 52: 113.

[6] LEVET A, KAVAZ E, ÖZDEMIR Y. An experimental study on the investigation of nuclear radiation shielding characteristics in iron−boron alloys [J]. Journal of Alloys and Compounds, 2020, 819: 152946.

[7] DUAN Yong-hua, LI Ping, ZHANG Min, PENG Ming-jun, MA Li-shi, SHU Bai-po. Corrosion behavior of Pb−39Mg−10Al−1.5B alloy in sodium halide solutions [J]. Journal of Alloys and Compounds, 2017, 792: 1108−1117.

[8] FENG Zhi-qi, BAO Wei-zong, BAO Long-ke, PENG Ming-jun, DUAN Yong-hua. Effects of yttrium on the microstructure and corrosion behavior of Pb−39Mg−10Al−1B−Y Alloys [J]. Journal of Materials Engineering and Performance, 2021, 30: 77−88.

[9] DUAN Yong-hua, SUN Yong, GUO Zhong-zheng, HE Jian-hong. Effects of B on Microstructure and shielding properties of Pb−Mg−Al−B shielding functional materials [J]. Journal of Functional Materials, 2012, 43: 334−337.

[10] BAO Wei-zong, BAO Long-ke, LIU Dan, QU De-yi, KONG Zhuang-zhuang, PENG Ming-jun, DUAN Yong-hua. Constitutive equations, processing maps, and microstructures of Pb−39Mg−10Al−1B−0.4Y alloy under hot compression [J]. Journal of Materials Engineering and Performance, 2020, 29: 607−619.

[11] DUAN Yong-hua. Hot deformation and processing map of Pb−Mg−10Al−1B alloy [J]. Journal of Materials Engineering and Performance, 2013, 22: 3049.

[12] DUAN Yong-hua, LI Ping, MA Li-shi, LI Run-yue. Dynamic recrystallization and processing map of Pb−30Mg−9Al−1B alloy during hot compression [J]. Metallurgical and Materials Transactions A, 2017, 48: 3419.

[13] DUAN Yong-hua, MA Li-shi, QI hua-rong, LI Run-yue, LI Ping. Developed constitutive models, processing maps and microstructural evolution of Pb−Mg−10Al−0.5B alloy [J]. Materials Characterization, 2017 129: 353.

[14] GU Dong-dong, XHANG Han, DAI Dong-hua, MA Cheng-long, ZHANG Hong-mei, LI Yu-xin, LI Shu-hui. Anisotropic corrosion behavior of Sc and Zr modified Al−Mg alloy produced by selective laser melting [J]. Corrosion Science, 2020, 170: 108657.

[15] YANG Ming-bo, ZHU Yi, PAN Fu-sheng, YANG Hui. Effects of minor Sr, Sn and Sc addition on as-cast microstructure and mechanical properties of ZA84 magnesium alloy [J]. Transactions of Nonferrous Metals Society of China, 2017, 708: 367−372.

[16] PENG Ying-hao, LIU Chong-yu, WEI Li-li, JIANG Hong-jie, GE Zhen-jiang. Quench sensitivity and microstructures of high-Zn-content Al−Zn−Mg−Cu alloys with different Cu contents and Sc addition [J]. Transactions of Nonferrous Metals Society of China, 2021, 31: 24−35.

[17] LIU Jia-ning, BIAN Dong, ZHENG Yu-feng, CHU Xiao, LIN Yu-lin, WANG Ming, LIN Ze-feng, LI Mei, ZHANG Yu, GUAN Shao-kang. Comparative in vitro study on binary Mg-RE (Sc, Y, La, Ce, Pr, Nd, Sm, Eu, Gd, Tb, Dy, Ho, Er, Tm, Yb and Lu) alloy systems [J]. Acta Biomaterialia, 2020, 102: 508−528.

[18] ZHANG Cheng, WU Liang, LIU Han, HUANG Guang-sheng, JIANG Bin, ATRENS A, PAN Fu-sheng. Microstructure and corrosion behavior of Mg−Sc binary alloys in 3.5 wt.% NaCl solution [J]. Corrosion Science, 2020, 174: 108831.

[19] HU Ping, SONG Rui, LI Xiao-jing, DENG Jie, CHEN Zhen-yu, LI Qin-wei, WANG Kuai-she, CAO Wei-cheng, LIU Dong-xin, YU Hai-liang. Influence of concentrations of chloride ions on electrochemical corrosion behavior of titanium−zirconium−molybdenum alloy [J]. Journal of Alloys and Compounds, 2017, 708: 367−372.

[20] SU Bao-xian, WANG Bin-bin, LUO Liang-shun, WANG Liang, SU Yan-qing, WANG Fu-xin, XU Yan-jin, HAN Bao-shuai, HUANG Hai-guang, GUO Jing-jie, FU Heng-zhi. The corrosion behavior of Ti−6Al−3Nb−2Zr−1Mo alloy: Effects of HCl concentration and temperature [J]. Journal of Materials Science & Technology, 2021, 74: 143−154.

[21] WANG Dong-peng, LI Xin, CHEN Zhen, WANG Shuai, WANG Yu-xin, LIU Wei-hong, LI Wei-li, XUE Rong-jie, LIU C T. Susceptibility of chloride ion concentration, temperature, and surface roughness on pitting corrosion of CoCrFeNi medium-entropy alloy [J]. Materials and Corrosion, 2022, 73: 106−115.

[22] KAPPES M A. Localized corrosion and stress corrosion cracking of stainless steels in halides other than chlorides solutions: A review [J]. Corrosion Reviews, 2020, 38: 1−24.

[23] LI Shi-da, ZHANG Xue-yu, ZHENG Shao-kui, DUAN Shou-peng, CUI Jun, ZHANG Hang-yu. $NaHCO_3$/Na_2CO_3 as an inhibitor of chloride-induced mild steel corrosion in cooling water: Electrochemical evaluation [J]. Journal of Industrial and Engineering Chemistry, 2021, 95: 235−243.

[24] THOMPSON T J. The technology of nuclear reactor safety [J]. Reactor Materials and Engineering, 1973, 2: 36−44.

[25] COHEN P. Water coolant technology of power reactors [M]. New York: Gorolon and Breach Science Publishers, 1969, 304−368.

[26] HU Ping, SONG Rui, LI Xiao-jing, DENG Jie, CHEN Zhen-yu, LI Qin-wei, WANG Kuai-she, CAO Wei-cheng, LIU Dong-xin, YU Hai-liang. Influence of concentrations of chloride ions on electrochemical corrosion behavior of titanium-zirconium-molybdenum alloy [J]. Journal of Alloys and Compounds, 2017, 708: 367−372.

[27] OSÓRIO W R, FREITAS E S, GARCIA A. EIS and potentiodynamic polarization studies on immiscible monotectic Al−In alloys [J]. Electrochimica Acta, 2013, 102: 436−445.

[28] OSÓRIO W R, PEIXOTO L C, MOUTINHO D J, GOMES L G, FERREIRA I L, GARCIA A. Corrosion resistance of directionally solidified Al−6Cu−1Si and Al−8Cu−3Si alloys castings [J]. Materials & Design, 2011, 32: 3832−3837.

[29] ZHANG X L, JIANG Z H, YAO Z P, SONG Y, WU Z D. Effects of scan rate on the potentiodynamic polarization curve obtained to determine the Tafel slopes and corrosion current density [J]. Corrosion Science, 2009, 51: 581−587.

[30] MCCAFFERTY E. Validation of corrosion rates measured by the Tafel extrapolation method [J]. Corrosion Science, 2005, 47: 3202–3215.

[31] DUAN Y H, SUN Y, HE J H, GUO Z Z, FANG D S. Corrosion behavior of as-cast Pb−Mg−Al alloys in 3.5% NaCl solution [J]. Corrosion, 2012, 68: 822−826.

[32] KUO Chun-liang, KAO Huan-jiun, WANG Hao. Novel design and characterization of surface modification in wire electrical discharge machining using assisting electrodes [J]. Journal of Materials Processing Technology, 2017, 244: 136−149.

[33] LIAO Cui-Jiao, LIU Qian, MA Xin-Zhou, LIU Jin-Hua. Relationship between surface heterogeneity and electrochemical interface behavior of the TiAl alloy electrode [J]. The Journal of Physical Chemistry C, 2019, 123: 473−484.

[34] ROSALBINO F, SCAVINO G, UBERTALLI G. Electrochemical corrosion behavior of LDX 2101® duplex stainless steel in a fluoride-containing environment [J]. Materials and Corrosion, 2020, 71: 2021−2018.

[35] DUAN Hui-juan, CUI Zi-xiang, XUE Yong-qiang, FU Qing-shan, CHEN Xing-hui, ZHANG Rong. Influence of particle size on electrochemical thermodynamics of nano-Au electrodes: Mechanism, factors, range and degree [J]. Electrochimica Acta, 2018, 281: 292−298.

[36] SHI Zhi-ming, LIU Ming, ATRENS ANDREJ. Measurement of the corrosion rate of magnesium alloys using Tafel extrapolation [J]. Corrosion Science, 2010, 52: 579−588.

[37] KHADKE P, TICHTER T, BOETTCHER T, MUENCH F, ENSINGER W, ROTH C. A simple and effective method for the accurate extraction of kinetic parameters using differential Tafel plots [J]. Scientific Reports, 2021, 11: 8974.

[38] CHEN Hao-tian, ELLIOTT JOSEPH R, LE Hao-nan, YANG Min-jun, COMPTON RICHARD G. Super-Nernstian Tafel slopes: An origin in coupled homogeneous kinetics [J]. Journal of Electroanalytical Chemistry, 2020, 869: 114185.

[39] PAJKOSSY T, JURCZAKOWSKI R. Electrochemical impedance spectroscopy in interfacial studies [J]. Current Opinion in Electrochemistry, 2017, 1: 53−58.

[40] CAI Shu-hua, LEI Ting, LI Nian-feng, FENG Fang-fang. Effects of Zn on microstructure, mechanical properties and corrosion behavior of Mg−Zn alloys [J]. Materials Science and Engineering C, 2012, 32: 2570−2577.

[41] MEYER Y A, BONATTI R S, BORTOLOZO A D, OSÓRIO WISLEI R. Electrochemical behavior and compressive strength of Al−Cu/*x*Cu composites in NaCl solution [J]. Journal of Solid State Electrochemistry, 2021, 25: 1303−1317.

[42] SINGH S, VERMA N. Fabrication of Ni nanoparticles-dispersed carbon micronanofibers as the electrodes of a microbial fuel cell for bio-energy production [J]. International Journal of Hydrogen Energy, 2015, 40: 1145−1153.

[43] SINGH S, VERMA N. Graphitic carbon micronanofibers asymmetrically dispersed with alumina−nickel nanoparticles: A novel electrode for mediatorless microbial fuel cells [J]. International Journal of Hydrogen Energy, 2015, 40:

5928−5938.
[44] JIA Xue-jiao, SONG Jiang-feng, QU Xiao-rong, CAO Fu-yong, JIANG Bin, ATRENS A, PAN Fu-sheng. Effect of scratch on corrosion resistance of calcium phosphate conversion coated AZ80 magnesium alloy [J]. Transactions of Nonferrous Metals Society of China, 2022, 32: 147−161.
[45] MA Yu-kun, WANG Ming-xing, LIU Ya-nan, CAI Bin. Microstructures and corrosion behaviors of Al−6.5Si−0.45Mg−*x*Sc casting alloy [J]. Transactions of Nonferrous Metals Society of China, 2022, 32: 424−435.
[46] PENG Can, LIU Yu-wei, GUO Ming-xiao, GU1 Tian-zhen, WANG Chuan, WANG Zhen-yao, SUN Cheng. Corrosion and pitting behavior of pure aluminum 1060 exposed to Nansha Islands tropical marine atmosphere [J]. Transactions of Nonferrous Metals Society of China, 2022, 32: 448−460.
[47] VIDA T A, FREITAS E S, CHEUNG N, GARCIA A, OSÓRIO W R. Electrochemical corrosion behavior of as-cast Zn-rich Zn−Mg alloys in a 0.06 M NaCl solution [J]. International Journal of Electrochemical Science, 2017, 12: 5264−5283.
[48] ELAISH R, CURIONI M, GOWERS K, KASUGA A, HABAZAKI H, HASHIMOTO T, SKELDON P. Effects of fluoride ions in the growth of barrier-type films on aluminium [J]. Electrochimica Acta, 2017, 245: 854−862.

Mg−39Pb−11.5Al−1B−0.4Sc 合金在 3.5% NaX (X = F, Cl, Br, I) 溶液中的腐蚀行为

冯芷琪，孙 缘，段永华，起华荣，彭明军

昆明理工大学 材料科学与工程学院，昆明 650093

摘 要：采用熔融法制备 Mg−39Pb−11.5Al− 1B−0.4Sc 合金，并利用 X 射线衍射仪(XRD)、扫描电子显微镜(SEM)、极化曲线测试和电化学阻抗谱 (EIS)分析合金在 3.5%(质量分数)NaX (X=F, Cl, Br, I)溶液中的腐蚀行为和机理。结果表明，Mg−39Pb−11.5Al−1B 合金的组成相为 α-Mg、Mg_2Pb、$Mg_{17}Al_{12}$ 和 AlB_2。Sc 的加入可以显著细化显微组织。Mg−39Pb−11.5Al−1B−0.4Sc 合金在 NaX 溶液中的耐腐蚀性顺序为 NaCl < NaBr < NaI < NaF。在 NaX(X = Cl, Br, I) 溶液的腐蚀过程中 Mg 先被溶解，然后 Mg_2Pb 被溶解，最后导致 $Mg_{17}Al_{12}$ 从基体脱落。Mg 和 Mg_2Pb 腐蚀产物分别为 $Mg(OH)_2$ 和 MgO。

关键词：Mg−39Pb−11.5Al−1B−0.4Sc 合金；卤素溶液；极化曲线；电化学阻抗谱；显微组织；耐腐蚀性

(Edited by Bing YANG)